



This is the accepted manuscript made available via CHORUS. The article has been published as:

## Plasmons in $mi$

$Z/mn > 2/mn >$  topological insulators

Yuling Guan, Stephan Haas, Henning Schlömer, and Zhihao Jiang

Phys. Rev. B **107**, 155414 — Published 11 April 2023

DOI: [10.1103/PhysRevB.107.155414](https://doi.org/10.1103/PhysRevB.107.155414)

# Plasmons in $\mathbb{Z}_2$ Topological Insulators

Yuling Guan,<sup>1,\*</sup> Stephan Haas,<sup>1</sup> Henning Schlömer,<sup>2,3</sup> and Zhihao Jiang<sup>4,†</sup>

<sup>1</sup>*Department of Physics and Astronomy, University of Southern California, Los Angeles, CA 91361*

<sup>2</sup>*Department of Physics and Arnold Sommerfeld Center for Theoretical Physics (ASC),*

*Ludwig-Maximilians-Universität München, Theresienstr. 37, München D-80333, Germany*

<sup>3</sup>*Munich Center for Quantum Science and Technology (MCQST), Schellingstr. 4, D-80799 München, Germany*

<sup>4</sup>*Department of Materials Science and Engineering,*

*University of Illinois at Urbana-Champaign, Urbana, IL 61801, USA*

(Dated: March 14, 2023)

We study plasmonic excitations in the Kane-Mele model, a two-dimensional  $\mathbb{Z}_2$  topological insulator on the honeycomb lattice, using the random phase approximation (RPA). In the topologically non-trivial phase, the model has conducting edge states that traverse the bulk energy gap and display spin-momentum-locking. Such a state of matter is called the quantum spin hall (QSH) phase, which is robust against time-reversal (TR) invariant perturbations. We find that in the QSH phase, gapless spin-polarized plasmons can be excited on the edges of the system. The propagation of these plasmons is chiral for each individual spin component and shows spin-momentum-locking for both spin components on the same edge. Moreover, we study the effect of external magnetic fields on the gapless edge plasmons. Specifically, out-of-plane magnetic fields delocalize edge plasmons propagating in one direction without affecting the other one, while an in-plane magnetic field can be applied to selectively excite a specific spin-plasmon branch with proper doping or gating to the system. Our findings may have potential applications in novel plasmonic and spintronic devices. We also investigate plasmons in the Kane-Mele model on a finite-sized diamond-shaped nanoflake and observe low-energy plasmons circulating the boundary of the material.

## I. INTRODUCTION

The experimental observation of the integer quantum Hall effect (IQHE) [1] has led to a fundamentally novel way of classifying electronic states via topological invariants. In the pioneering work of Thouless, Kohmoto, Nightingale, and den Nijs [2] (TKNN), the topological invariant for the IQHE was identified as an integer called the Chern number. Here, non-trivial topology is attributed to a broken time reversal (TR) symmetry [3]. In the context of TR-invariant systems, where the Chern number vanishes, Kane and Mele [4, 5] introduced another  $\mathbb{Z}_2$  topological classification which distinguishes the quantum spin Hall (QSH) phase from the trivial insulating phase. The QSH phase is characterized by spin-momentum-locked topological surface states traversing the bulk energy band gap. Kramers theorem [6] guarantees the degeneracy of energy bands at TR invariant momenta (TRIM) and forbids gap opening on the surface from any TR-invariant perturbation [7].

While the topological electronic properties have been extensively studied in the past few decades [8–19], the behavior of collective excitations, such as plasmons [20–30] and magnons [31–33] in topologically non-trivial systems is drawing increasing attention as well. Our previous studies have found that plasmonic excitations in the

Su-Schrieffer-Heeger (SSH) model [34–36] and the Haldane model [36] are clearly affected by the underlying electron topology, and consequently display characteristic behavior such as gapless spectra, localized modes on the sample surface, and robustness against appreciable disorder. While these models consider spinless electrons, in  $\mathbb{Z}_2$  topological insulators (TIs) it is necessary to treat electrons as spinors due to possible spin-mixing couplings. In fact, plasmons in such systems have been studied on surfaces of two-dimensional (2D) [29] and three-dimensional (3D) [20, 23, 29, 37] TIs. Due to the spin-momentum-locking of the conducting edge states in  $\mathbb{Z}_2$  TIs, these surface plasmons are spin polarized along certain directions. For this reason, they are called “spin-plasmons”, with novel applications in plasmonics and spintronics [38]. Moreover, spin-polarized plasmons were also reported in the two-dimensional electron gas that are observed in Raman-scattering experiments [39], and in spin-polarized graphene that shows long lifetime dispersing in its undamped regime [40]. However, we are not aware of any studies of how such surface spin-plasmons can be engineered and tuned by e.g. the application of electromagnetic fields. Considering the potentially significant applications of spin-plasmons, we believe it is useful to report here our studies on controlling surface spin-plasmons.

In this paper, we consider the Kane-Mele model [4], a paradigmatic model of 2D  $\mathbb{Z}_2$  TIs, on a ribbon structure as in Fig.1(b). In its TR-symmetric QSH phase, we observe spin-polarized gapless edge plasmons displaying chirality, spin-momentum-locking and spin-edge-locking that are inherited from the topology and symmetry of the underlying single-electron states. We find that these

---

\* yulinggu@usc.edu

† zjiang22@illinois.edu; The research work presented in this paper started when the author was a PhD candidate in the Department of Physics and Astronomy at University of Southern California (USC), Los Angeles, CA 91361. The author thanks USC for the support during that time.

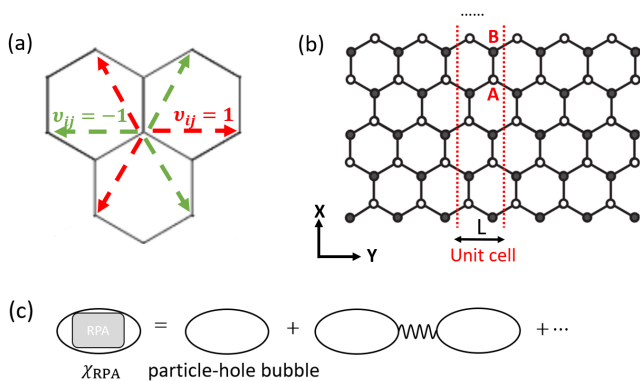


FIG. 1. (a) Determination of the sign  $\nu_{ij}$  for the spin-orbit coupling term in the Kane-Mele model on a Honeycomb lattice. (b) Illustration of Kane-Mele model on a ribbon structure with zigzag terminations. Two atomic species A and B are non-equivalent with a non-zero onsite energy  $t_v$ . Two dashed red lines define a unit cell that is repeated along the Y-direction with period  $L$ . (c) Diagrammatic representation of the Dyson series for RPA susceptibility function. The particle-hole bubble diagram represents the non-interacting polarization function and the wiggly line represents the bare Coulomb interaction.

plasmons are sensitive to external magnetic fields applied in different directions, which can therefore be used as a practical technique to control them, although the field breaks the TR symmetry such that some topological features of these plasmons are lost. Specifically, we show that an out-of-plane magnetic field can be applied to tune surface plasmon localization, and an in-plane magnetic field can be used to selectively excite plasmons with certain spin polarization. Moreover, we calculate the plasmonic excitation spectrum in real-space in a diamond-shaped Kane-Mele model and observe edge plasmons circulating the sample. The single-electron topological properties of this model have recently been investigated in [41].

The remainder of this paper is organized in the following way. In Sec. II, we introduce the random phase approximation (RPA) method applied to the ribbon structure for calculating the dielectric response and plasmonic excitations. In Sec. III, we present detailed results of plasmonic excitations in the Kane-Mele model. Plasmons in the original Kane-Mele ribbon structure are firstly introduced, followed by two variant scenarios when the original system is exposed to an external magnetic field applied in the out-of-plane direction and the in-plane direction. This is followed by a discussion of plasmons in real space on a diamond-shaped Kane-Mele model with open boundaries. Finally, we conclude our study, proposing potential applications of these results and give future research directions in Sec. IV.

## II. METHOD

In order to study plasmonic excitations, we calculate the dielectric function within the random phase approximation (RPA). The RPA dielectric function has traditionally been introduced in momentum space for the homogeneous electron gas [42, 43], as well as recently been formulated fully in real space to study non-translational-invariant systems [34, 35, 44, 45]. In RPA, the charge susceptibility function is considered as the Dyson series of the non-interaction polarization function linked by the bare Coulomb interaction, whose diagrammatic representation is shown in Fig.1(c). This is analogous to evaluating the interacting Green function from the non-interacting one using the self-energy. In this paper, we mainly focus on ribbon structures, which are periodic in the longitudinal direction while finite-sized in the transverse direction (Fig.1(b)). Therefore, we adopt a combined treatment of both the real- and momentum space as detailed below.

Generically, as indicated in Fig. 1 (b), the unit cell spans the entire width of the ribbon (along X-direction) and is repeated periodically along the Y-direction. We denote the position and the spin of the  $i$ -th atom in the unit cell as  $\vec{\tau}_i$  and  $\vec{\sigma}_i$ . By Fourier transformation along the Y-direction, we can construct a tight-binding basis  $\{|\mu\rangle \equiv |\vec{\tau}\rangle \otimes |\sigma\rangle, \vec{\tau} = \vec{\tau}_1, \vec{\tau}_2, \dots, \vec{\tau}_N \text{ and } \sigma = +, -\}$  for each  $k_y$ , supposing there are  $N$  atoms in the unit cell. Using this, we can express the non-interacting polarization function as a matrix, whose element indexed by  $\mu$  and  $\mu'$  is given by [45]

$$\chi_0(\omega, q_y)_{\mu\mu'} = \frac{1}{L} \sum_{k_y, n, n'} \frac{f(E_n^{k_y}) - f(E_{n'}^{k_y+q_y})}{\omega + i\gamma + E_n^{k_y} - E_{n'}^{k_y+q_y}} \times \psi_{n\mu}^{k_y} (\psi_{n\mu'}^{k_y})^* (\psi_{n'\mu}^{k_y+q_y})^* \psi_{n'\mu'}^{k_y+q_y}, \quad (1)$$

where  $\omega$  is the frequency and  $q_y$  is the momentum transfer in Y-direction.  $L$  is the volume of the unit cell in the periodic direction as shown in Fig.1.  $E_n^{k_y}$  and  $\psi_{n\mu}^{k_y}$  are the eigenenergy and the component of the eigenstate on the  $\mu$ -th spin orbital in the tight-binding basis, for the electronic state in the  $n$ -th band and with momentum  $k_y$ . They can be computed from diagonalization of the tight-binding Hamiltonian  $H(k_y)$  written in the same basis introduced above.  $f(\cdot)$  is the Fermi-Dirac distribution function, whose zero temperature limit is applied in all calculations in this paper. Moreover, we introduce a finite broadening parameter  $\gamma$  which is set to be 0.01 eV.

On the other hand, we consider electron-electron Coulomb interaction which is also Fourier transformed along the Y-direction, namely,  $V(q_y)$ . Using the same basis and assuming that the Coulomb interaction only depends on the real-space coordinates of two sites [46], we have

$$V_{\mu\mu'}(q_y) = \begin{cases} 2e^2 * K_0(|q_y||x - x'|)/\kappa, & \text{if } \vec{\tau} \neq \vec{\tau}', \\ U_0/\kappa, & \text{if } \vec{\tau} = \vec{\tau}'. \end{cases} \quad (2)$$

Here  $K_0(\cdot)$  is the zeroth modified Bessel function of the second kind. This form of the Coulomb interaction is referred from [47]. For the onsite Coulomb interaction, the formula for point charges lead to divergent result. So, we choose to parametrize it as  $U_0 = 17.38$  eV using the value from Ref. [34] where electrons were described using two-dimensional Gaussian wavefunctions. Additionally,  $\kappa$  is the dielectric constant of the background medium which is set to be  $\kappa = 1$  (the vacuum) unless otherwise specified.

We can then derive the dielectric matrix within RPA as

$$\epsilon_{\text{RPA}}(\omega, q_y) = \mathbf{I} - V(q_y) \chi_0(\omega, q_y), \quad (3)$$

form which we can further extract the electron energy loss spectrum (EELS) by

$$\text{EELS}(\omega, q_y) = \max_i \left\{ -\text{Im} \left[ \frac{1}{e_i(\omega, q_y)} \right] \right\}, \quad (4)$$

where  $e_i(\omega, q_y)$  is the  $i$ -th eigenvalue of  $\epsilon_{\text{RPA}}(\omega, q_y)$ . Plasmonic excitations are identified as peaks in  $\text{EELS}(\omega, q_y)$ . Meanwhile, the real-space charge distribution patterns of plasmon modes can also be obtained utilizing the right eigenvector of the dielectric matrix  $\epsilon_{\text{RPA}}(\omega, q_y)$ . The method is similar to the one reported in [34] for the full real-space RPA calculation. Suppose that  $e_m(\omega_p, q_y)$  is the selected eigenvalue indicating a plasmon mode at  $\omega_p$ , then the real-space charge distribution pattern of this mode can be obtained by

$$\rho_0(\omega_p, q_y) = \chi_0(\omega_p, q_y) \xi_m(\omega_p, q_y), \quad (5)$$

with  $\xi_m(\omega_p, q_y)$  is the right eigenvector corresponding to  $e_m(\omega_p, q_y)$ . In fact, we can also obtain the second EELS (2nd-EELS) by selecting the second maximum in Eq. (4), which will provide information about degeneracy of plasmon modes. In this paper, we will always consider the maximum EELS unless otherwise specified.

### III. MODELS AND RESULTS

#### A. Chiral edge spin-plasmons in the Kane-Mele ribbon structure

The Kane-Mele model on a honeycomb lattice is given by the Hamiltonian [4]

$$\begin{aligned} H = & t \sum_{\langle i,j \rangle} c_i^\dagger c_j + it_{\text{SO}} \sum_{\langle\langle i,j \rangle\rangle} \nu_{ij} c_i^\dagger s^z c_j \\ & + it_R \sum_{\langle i,j \rangle} c_i^\dagger (\mathbf{s} \times \hat{\mathbf{d}}_{ij})_z c_j + t_v \sum_i \xi_i c_i^\dagger c_i. \end{aligned} \quad (6)$$

Here  $c_i^\dagger = (c_{i\uparrow}^\dagger, c_{i\downarrow}^\dagger)$  and  $c_i = (c_{i\uparrow}, c_{i\downarrow})$  are electron creation and annihilation operators. The first term is the hopping between nearest neighbor sites denoted as  $\langle i, j \rangle$ .

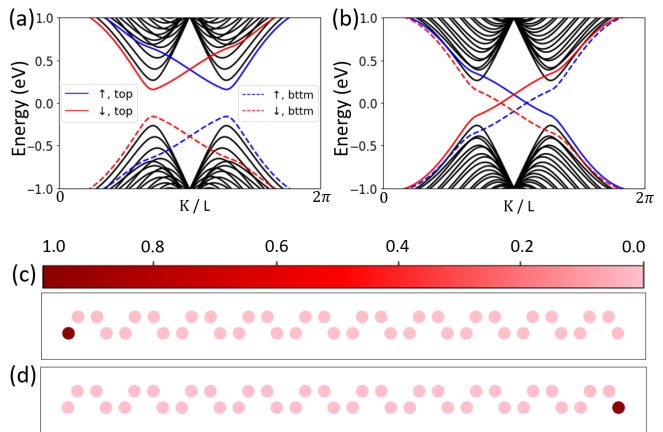


FIG. 2. Electronic band structure of the Kane-Mele model on a ribbon with zigzag terminations. (a) Trivial insulating phase with  $t_{\text{SO}} = 0.05t$  and  $t_v = 0.4t$ . (b) Quantum Spin Hall (QSH) phase with  $t_{\text{SO}} = 0.05t$  and  $t_v = 0.1t$ . Conducting edge states traversing the bulk energy band gap are observed. Two spin components are represented by blue and red bands; two edges are represented by solid and dashed bands. (c) and (d) are modular square of electronic wavefunctions of the two spin-up edge states at the momentum  $K = 1.01\pi/L$ . They are strongly localized on two opposite edges.

The second term describes the mirror symmetric intrinsic spin-orbit coupling involving next nearest neighbor sites  $\langle\langle i, j \rangle\rangle$ . The sign  $\nu_{ij}$  depends on the orientation of the hopping as illustrated in Fig. 1(a). Mathematically, it can be determined by  $\nu_{ij} = (2/\sqrt{3}) (\hat{\mathbf{d}}_1 \times \hat{\mathbf{d}}_2)_z$ , where  $\hat{\mathbf{d}}_1$  and  $\hat{\mathbf{d}}_2$  are unit vectors along the two bonds that traverse from the  $j$ th site to the  $i$ th site.  $s_z$  is the diagonal Pauli matrix.  $t_{\text{SO}}$  is the amplitude for spin-orbit interaction and can be determined by second-order perturbation theory calculations [48–51]. The third term is the Rashba coupling between nearest neighbor sites. It introduces an off-diagonal spin mixing term that can arise from applying a perpendicular electric field or placing the sample on a substrate. Its amplitude  $t_R$  can be experimentally measured [52, 53]. The last term is a staggered sublattice potential ( $\xi_i = \pm 1$ ) on site A and B [Fig. 1(b)], which breaks the in-plane twofold rotation symmetry for non-zero  $t_v$ . In a ribbon structure of Fig. 1(b), it breaks the symmetry between two edges as the top and bottom edge are terminated at different atomic species. In our numerical calculations, we set the nearest neighbor hopping parameter  $t = 1$  eV and all other energies are scaled in the unit of  $t$ . We also set  $t_R = 0$  for simplicity, such that the topological sector of the model can be tuned by the ratio of  $t_{\text{SO}}$  and  $t_v$ . In this case, the spin-up and spin-down electrons are originally decoupled. The case with non-zero  $t_R$  is presented in Appendix D and no significant effects are observed as long as  $t_R$  is sufficiently small.

We focus on the Kane-Mele model on the ribbon structure with zigzag terminations as illustrated in Fig. 1(b).

For  $t_R = 0$ , the model has a bulk energy band gap  $E_g = |6\sqrt{3}t_{\text{SO}} - 2t_v|$  [4] that vanishes when  $t_v = 3\sqrt{3}t_{\text{SO}}$ . For  $t_v > 3\sqrt{3}t_{\text{SO}}$ , the system is in the trivial insulating phase, while for  $t_v < 3\sqrt{3}t_{\text{SO}}$  it is in the topologically non-trivial quantum spin Hall (QSH) phase [4]. A topological phase transition occurs at  $t_v = 3\sqrt{3}t_{\text{SO}}$  characterized by band inversion at this critical gap-closing point [54]. This distinction is illustrated via the electronic single particle band structure in Fig. 2. In Fig. 2(a), we choose  $t_{\text{SO}} = 0.05t$  and  $t_v = 0.4t$  (the trivial insulating phase) and observe no edge states traversing the bulk energy gap. In Fig. 2(b) (with  $t_{\text{SO}} = 0.05t$  and  $t_v = 0.1t$ , i.e. the system is in the QSH phase), we observe conducting edge states crossing the energy gap. For any energy within the bulk band gap, there is one TR edge-states pair on each edge, indicating a non-trivial (odd)  $\mathbb{Z}_2$  topological order. The conducting edge states for spin-up and spin-down electrons on each edge propagate in opposite directions, which is a characteristic property called “spin-momentum-locking” in the QSH phase. We plot the modular square of the wave functions  $|\psi|^2$  for two spin-up electronic edge states at zero energy (Figs. 2(c) and (d)), confirming that they are localized on two opposite edges. The same properties apply for spin-down electronic edge states. Due to the non-zero  $t_v$  in the calculation, energy spectra of conducting edges states on the top edge (solid lines) and the bottom edge (dashed lines) are shifted.

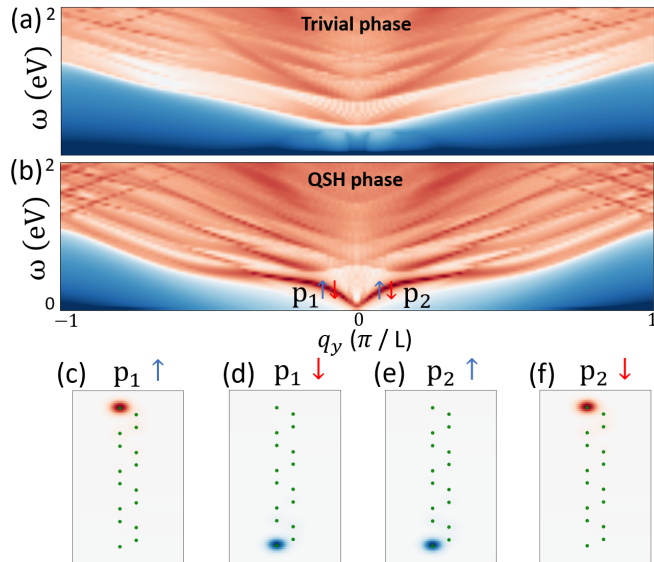


FIG. 3. Electron energy loss spectra (EELS) of the Kane-Mele model on a ribbon structure in (a) the trivial insulating phase and (b) the in the QSH phase. Gapless spin-plasmons are observed on the edges of the QSH system. (c-f) show real-space charge modulation patterns of the spin-up plasmon at  $P_1$  ( $q_y = \pi/8L$ ), the spin-down plasmon  $P_1$ , the spin-up plasmon at  $P_2$  ( $q_y = -\pi/8L$ ) and the spin-down plasmon at  $P_2$ . The excited energy is  $0.326t$ . Red and blue in the modulations represent the positive and negative charges.

We now analyze the plasmonic excitations in the Kane-Mele ribbon structure. Firstly, we show that *gapless edge plasmons* can be excited in the QSH phase, but not in the trivial insulating phase. In Figs. 3(a) and (b), we plot the plasmon dispersions for both phases. We observe that in the QSH phase, gapless low-energy plasmons emerge due to the existence of the conducting edge states observed in the single-electron band structure (see Appendix. A for a detailed analysis of the relation between both). These plasmons are localized on the edges of the ribbon, as confirmed by the real-space charge distribution patterns of some typical modes shown in Figs. 3(c-f). In contrast, gapless edge plasmons are absent in the trivial insulating phase.

Secondly, we find that gapless edge plasmons are spin-resolved and inherit *chirality* as well as *spin-momentum-locking* from the QSH electronic structure. *Chirality* of the gapless edge plasmons can be detected by focusing on each individual spin component. In the spin-decoupled QSH regime ( $t_R = 0$ ), each spin component behaves effectively as a non-trivial Chern insulator displaying chiral edge current flow. We analyze in detail the inheritance of chirality from the electronic structure to the plasmonic excitations for the spin-up component, while the spin-down component can be understood in the exactly same way. The spin-up edge current propagates uni-directionally with positive (negative) momentum on the bottom (top) edge, as indicated by the positive (negative) slope of the dashed (solid) blue edge-states energy dispersion in Fig. 2(b). This property is inherited by the plasmons in the sense that the spin-up edge plasmons with positive (negative) momenta  $q_y$  can only stay on the bottom (top) edge, as indicated by the mode profile of “ $P_2 \uparrow$ ” in Fig. 3(e) (“ $P_1 \uparrow$ ” in Fig. 3(c)). This can be understood by noticing that for the positive (negative) momentum transfer  $q_y$ , spin-up electronic transitions can only occur within the dashed (solid) blue band in Fig. 2(b), along which all electronic states are localized on the bottom (top) edge of the ribbon. It is true that electronic transitions with positive (negative)  $q_y$  can also occur within the solid (dashed) red band. However, this band includes spin-down electronic states localized on the top (bottom) edge of the ribbon, which have negligible interference with the dashed (solid) blue band of spin-up electrons on the bottom (top) edge due to their large real-space separation. On the other hand, *spin-momentum-locking* of gapless edge plasmons can be inferred by focusing on each individual edge. On the top edge, spin-up plasmons can only be excited with negative momentum  $q_y$  (Fig. 3(c)), whereas spin-down plasmons are restricted to positive momenta. On the bottom edge, we find the opposite behavior for the two spin components. The reason for the spin-momentum-locking of gapless edge plasmons can also be understood by analyzing the restricted transitions within each conducting electronic bands in Fig. 2(b). As noticed from Fig. 3(b), in the original Kane-Mele model with TR symmetry, the plasmon dispersions also display “TR symmetry” in the sense that the rela-

tion  $\omega_{\uparrow}(q_y) = \omega_{\downarrow}(-q_y)$  (or  $\omega_{\uparrow}(-q_y) = \omega_{\downarrow}(q_y)$  on the other edge) holds. Later we will see that this relation is broken with applied external magnetic field which breaks the TR symmetry.

Lastly, if we excite gapless edge plasmons at a specific momentum  $q_y$ , TR symmetry and spin-momentum-locking in the QSH phase transform into a new special property of these plasmons, which we will call *spin-edge-locking*. For instance, using an external excitation field with a specific positive  $q_y$ , spin-up plasmons can only be excited on the bottom edge (Fig. 3(e)), while spin-down plasmons can only be excited on the top edge (Fig. 3(f)). This property opens up possibilities for plasmon engineering using these gapless edge spin-plasmons by gating, doping or substrate manipulation on the edges. For instance, here we propose a way to energetically separate spin-up edge plasmons and spin-down edge plasmons via substrates engineering. As we know that plasmon dispersion sensitively depends on Coulomb interactions which can be tuned by the local screening environment [55], by applying different dielectric substrates on the top edge and the bottom edge of the ribbon, we can tune the energies of spin-up plasmons and spin-down plasmons separately. They can then be selectively excited by choosing external excitation field with corresponding frequency  $\omega_{\text{top}}$  or  $\omega_{\text{bottom}}$ .

In summary, we have investigated plasmonic excitations in Kane-Mele ribbon structure in both the trivial phase and the QSH phase. In the QSH phase we have observed spin-polarized gapless edge plasmons which are obviously absent in the trivial phase. Moreover, these plasmons display characteristic properties of strong localization, chirality for each spin component, spin-momentum-locking on each edge, and spin-edge-locking for each individual excitation  $(\omega, q_y)$ . These properties are analyzed to be inherited from the single-electron topology of the underlying model. Therefore, gapless edge plasmons with above characteristic properties can be regarded as a topological signature of collective excitations in TR-invariant QSH insulators.

## B. Tuning edge plasmons via external magnetic fields

In this section, we study the Kane-Mele model in the presence of external magnetic field. The original model Hamiltonian is modified by adding a Zeeman energy term induced by the external magnetic field  $\mathbf{B}$ , which is given here as

$$H^Z = H_{\text{KM}} + \sum_i c_i^{\dagger} \mathbf{B} \cdot \mathbf{s} c_i. \quad (7)$$

$H_{\text{KM}}$  refers to the Kane-Mele model Hamiltonian from Eq. 6. As we shall see in the following, although applying magnetic field breaks the TR symmetry, it can be useful to tune the edge plasmons excited in the Kane-Mele model. The tuning effect depends on the direction

of applied Zeeman field.

### 1. Control of edge plasmons localization via $\mathbf{B}_z$ field

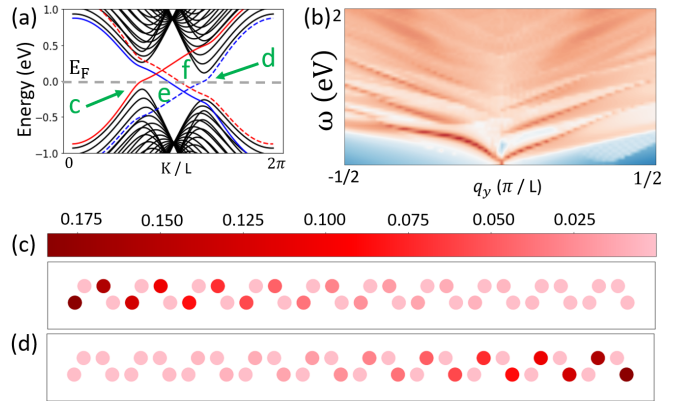


FIG. 4. (a) Electron band structure, and (b) plasmon dispersions, of the QSH Kane-Mele ribbon structure in presence of an out-of-plane magnetic field  $\mathbf{B}_z$ . (c) and (d) are modular square of electronic eigenstates at “c” and “d” points marked in the electron band structure (a).

We first consider the external magnetic field applied in the out-of-plane direction, namely  $\mathbf{B}_z = B_z \hat{\mathbf{z}}$ . In Fig. 4(a), we show the electronic band structure of the QSH Kane-Mele ribbon when  $B_z = 0.15t$ . There are three main effects to be addressed due to the presence of the magnetic field. Firstly, introducing  $\mathbf{B}_z$  does not open a gap on the edge of the system. For each spin component, conducting edge states crossing over the bulk band gap remain. Therefore, gapless edge plasmons are preserved, which is shown by the EELS in Fig. 4(b). Secondly, the field breaks the TR symmetry on each edge because the system is magnetized. This will correspondingly break TR symmetry in the corresponding plasmon branches. The relation  $\omega_{\uparrow}(q_y) = \omega_{\downarrow}(-q_y)$  is explicitly broken, as indicated by the asymmetric dispersion for  $q_y \leq 0$  in Fig. 4(b). Such an asymmetric property of plasmons may find potential applications in non-reciprocal plasmonic and spintronic devices. Thirdly, although the  $\mathbf{B}_z$  field does not destroy gapless edge plasmons, the real-space localization of these edge plasmons can be affected. Particularly, significant delocalization for plasmons with small positive  $q_y$  is expected, because they are dominated by single electron states near “c” and “d” points (marked in Fig 4(a)) crossed by the Fermi level. As we can see, these two points are very close to bulk bands, such that their wave functions are delocalized (cf. Figs. 4(c) and (d), Figs. 2(c) and (d)). In contrast, we do not expect significant delocalization effects to appear for plasmons with small negative  $q_y$ , because states “e” and “f” are still deep in the gap.

We investigate the delocalization effect on positive  $q_y$  edge plasmons in more detail. Here we select modes along

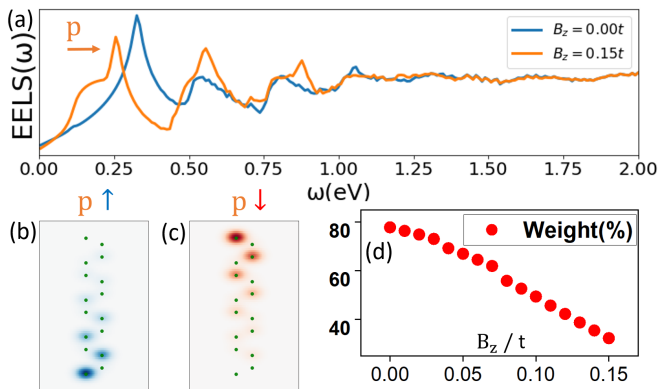


FIG. 5. (a) EELS of the QSH Kane-Mele ribbon structure evaluated along the momentum transfer  $q = \pi/8L$  with and without an external magnetic field  $\mathbf{B}_z = 0.15t\hat{z}$ . Spin-orbit interaction for the numerical calculation here is set to be  $t_{SO} = 0.05t$ . (b) and (c) are real-space charge modulation patterns of two spin-plasmons excited at “P” (energy:  $0.249\text{ eV}$ ) in the presence of the external field  $\mathbf{B}_z$ . They are delocalized into the bulk. (d) shows a decreasing weight of charges on the edge for the plasmon mode “P” with increased strength of the field  $\mathbf{B}_z$ .

$q_y = \pi/8L$  and plot the EELS as a function of  $\omega$ , namely,  $\text{EELS}(q_y = \pi/8L, \omega)$ . This is given in Fig. 5(a) for both  $B_z = 0$  (no magnetic field) and  $B_z = 0.15t$ . The first mode in each spectrum is the edge plasmon. As we can see, introducing  $B_z$  changes the excitation energy of the edge plasmon, an effect induced by the changed electronic band structure. More interestingly, the mode localization in the real space is strongly affected by  $B_z$ . In Figs. 5(b) and (c), we show the real-space charge modulation patterns of spin-up and spin-down plasmons excited at “p”. While the “spin-edge-locking” character remains, both modes strongly delocalize compared to their counterparts in Figs. 3(e) and (f) without external magnetic fields. In fact, localization of edge plasmons can be gradually changed by tuning the field strength  $B_z$ . In Fig. 5(d), we show how the weight of charges localized on the edge decreases with an increased value of  $B_z$  in the range of 0 to  $0.15t$ . This observation indicates a way to control edge plasmons localization via an external  $\mathbf{B}_z$  field. We note that the tuning effect depends on the original bulk band gap of the system. If the original bulk band gap is large, a small external field  $B_z$  will not have a big influence on the plasmon spectrum and mode localization. Detailed analysis for this case is given in Appendix B.

## 2. Selective excitation of spin-polarized plasmons with applied $\mathbf{B}_x$ field

We now turn to the QSH Kane-Mele model in the presence of an in-plane magnetic field  $\mathbf{B}_x = B_x\hat{x}$  applied in  $x$ -direction. This induces an off-diagonal on-site spin-flip term that violates the time-reversal symmetry, which opens a gap on each edge of  $E_g = 2B_x$  (Fig. 6(a)). For

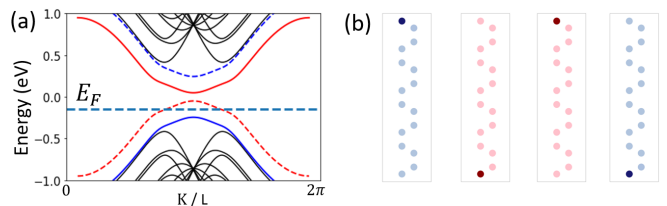


FIG. 6. Electronic band structure of the Kane-Mele ribbon structure in the presence of an in-plane magnetic field  $\mathbf{B}_x = 0.15t\hat{x}$ . An energy gap is opened on each edge due to the spin-flip TR-broken term. Four bands in the middle correspond to spin-up and spin-down electronic states localized on the top and bottom edges, represented in the same way as in Fig. 2. (b) Modular square of electronic eigenstates of the middle four bands at  $K = 1.01\pi/L$ . The sub-figures are ordered from low energy to high energy. Strong localization character is still preserved in the presence of  $\mathbf{B}_x$  field.

strong enough  $B_x$ , the model is completely gapped at zero energy. Gapless edge plasmons will therefore vanish if we keep the Fermi level at  $E_F = 0\text{ eV}$ . However, the localization character of electron eigenstates on these bands is still preserved, as long as these bands still extend deeply in the bulk energy gap. This can be confirmed the modular square of the four electronic eigenstates at  $k = 1.01\pi/L$  plotted in Fig. 6(b).

The above property of the electronic structure in the presence of  $\mathbf{B}_x$  implies a way to selectively excite gapless edge plasmons with specific spin polarization. As we can see, due to the gap opening on each edge, the spin-up electron band and the spin-down electron band are energetically separated. We can tune the Fermi level by doping [56, 57] or gating [58] the system such that  $E_F$  crosses one band of a specific spin polarization, as illustrated in Fig. 6(a). In this case, the spin-down electron band on the bottom edge (the dashed red line) becomes conducting. Therefore, gapless edge plasmons can just be excited for spin-down electrons on the bottom.

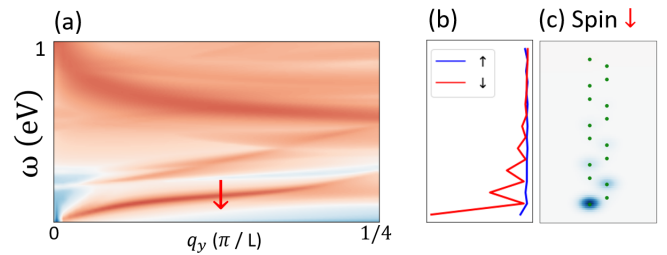


FIG. 7. (a) EELS of the Kane-Mele ribbon structure with a shifted Fermi level  $E_F = -0.15t$  and in the presence of an in-plane magnetic field  $\mathbf{B}_x = 0.15t\hat{x}$ . Gapless edge plasmons are observed for spin-down component only. (b) Spin projection and (c) real-space charge modulation pattern of the plasmon mode marked by the red down-arrow in (a), which with  $q_y = \pi/8L$  and energy =  $0.146\text{ eV}$ .

To illustrate this, we calculate the EELS of the Kane-Mele ribbon in presence of a  $\mathbf{B}_x$  field with the Fermi

level set to be  $E_F = -0.15t$  (crossing the dashed red band). The result is plotted in Fig. 7(a), from which we can clearly see a gapless plasmon dispersion branch. As expected before, these plasmons are of spin-down electrons localized on the bottom edge of the ribbon. For instance, we show the real-space charge modulation pattern of the plasmon mode at  $q_y = \pi/8L$  (indicated by the red down-arrow) in Fig. 7(c). This plasmon is indeed an edge mode localized on the bottom edge. Moreover, we project this charge distribution onto each spin component and show them in Fig. 7(b). We observe that the mode is strongly spin-polarized, whereby the spin-down component dominates. It is worth mentioning that in previous sections of non-gapped models (no matter with  $\mathbf{B}_z$  field or not), gapless edge plasmons always come in pairs of spin-up component and spin-down component (see Fig. 3(b) and Fig. 4). In the present case, the phenomenon is fundamentally different, as we only have one spin component of gapless edge plasmons excited. The in-plane magnetic field here preserves the mirror symmetry  $\mathcal{M}_y$  [41] such that the energy bands remain symmetric, however, the relation  $\omega_\uparrow(q_y) = \omega_\downarrow(-q_y)$  is still broken due to the complete absence of one spin-plasmon branch. Here we should clarify that the realization of selective excitation of spin-plasmons is at the cost of losing chirality. From the electronic structure in Fig. 6, we can see that the back-scattering channel within the conducting dashed red band is open. Therefore, spin-down plasmons localized on the bottom edge with negative  $q_y$  can also be excited. This is distinct from the situation with  $\mathbf{B}_z$ , where we have observed non-reciprocity.

### C. Real-space edge plasmons in Kane-Mele model on a diamond-shaped nanoflake

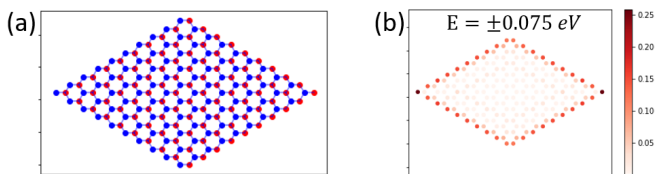


FIG. 8. (a) Structure of the Kane-Mele model on a diamond-shaped honeycomb lattice nanoflake with zigzag edges. (b) Modular square of degenerate single-electron edge states of the model at energies  $\pm 0.075$  eV.

In this section, we study plasmons in the Kane-Mele model on a different structure - a diamond-shaped nanoflake of honeycomb lattice with open boundaries of zigzag termination. This structure is illustrated in Fig.8(a) with nearest neighbour bond length of  $a = 1.42\text{\AA}$ . We study the model in the QSH phase parameterized with  $t_{SO} = 0.2t$  and  $t_v = 0$ . In this case, we find low-energy edge states shown in Fig.8(b). Next, we study the plasmonic excitations in the model using the full real-space RPA method introduced in [35]. The sys-

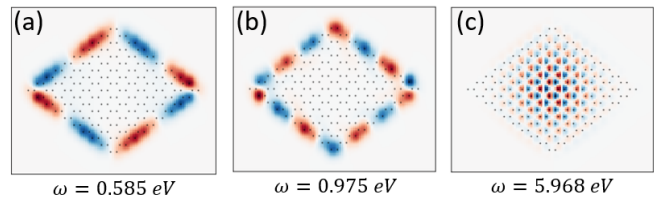


FIG. 9. Real-space charge modulation patterns of typical plasmon modes in the QSH Kane-Mele model on a diamond-shaped nanoflake. (a) and (b) are low-energy edge plasmons excited at  $\omega = 0.585$  eV and  $\omega = 0.975$  eV. (c) is a high-energy bulk plasmon excited at  $\omega = 5.968$  eV.

tem supports both low-energy edge plasmons and high-energy bulk plasmons. We show three typical modes in Fig. 9. In the Figs. 9(a) and (b) we see two edge modes with different energies and wave-vectors. This indicates that low-energy edge plasmons are dispersive. The edge plasmons are extremely localized along the boundary of the nanoflake. A typical bulk plasmon mode at high energy is shown in Fig. 9(c) with charges oscillating inside the material.

## IV. CONCLUSIONS

In conclusion, we have performed a detailed study on plasmons in the Kane-Mele model with theoretical analysis and numerical calculations. Plasmonic excitations are identified from the electron energy loss spectrum derived from the dielectric function calculated within the random phase approximation (RPA). We have mainly considered the Kane-Mele model on a ribbon structure in the topologically non-trivial QSH phase where spin-polarized gapless edge plasmons have been observed. For each spin-polarization, plasmons propagate unidirectionally on the edges of the ribbon. On the same edge, spin-up plasmons and spin-down plasmons always propagate in opposite directions. For a specific momentum transfer  $q_y$  along the longitudinal direction of the ribbon, both spin-polarized plasmons can be excited, but localized on opposite edges. We summarize these three properties as *chirality*, *spin-momentum-locking*, and *spin-edge-locking* of plasmons in QSH insulators. Plasmons in the QSH phase are sensitive to external magnetic fields. Applying an out-of-plane magnetic field  $\mathbf{B}_z$  breaks the TR symmetry by effectively magnetizing the material. However, it does not open a gap without introducing any non-TR-invariant spin-mixing term. Therefore, spin-polarized gapless edge plasmons remain, but the dispersion spectrum is no longer TR symmetric. We have found that increasing the field strength of  $\mathbf{B}_z$  will gradually delocalize edge plasmons in one direction, but does not significantly affect edge plasmons in the opposite direction. On the other hand, applying an in-plane magnetic field  $\mathbf{B}_x$  along the transverse direction of the ribbon opens a gap on each edge by breaking the TR symmetry with onsite spin-flip term.

In this case, spin-up and spin-down electron bands on the same edge are energetically shifted. By tuning the chemical potential via proper doping or gating, we can selectively make one spin-polarized edge band conducting and therefore excite gapless edge plasmons with specific spin-polarization. However, we have clarified that these edge plasmons are no longer chiral due to opened back-scattering channel. Our results imply that spin-polarized plasmons in 2D QSH topological insulators can be manipulated by external magnetic field. Besides the ribbon structure, we have also investigated plasmons of the QSH Kane-Mele model on a diamond-shaped nanoflake with open boundaries. We have observed low-energy edge plasmons circulating the sample, which can also be interpreted as a topological signature of the model in its collective excitations.

We would expect spin-polarized plasmons studied in our work could possibly be detected by magneto-optic Kerr effect (MOKE) in experiments [59]. Moreover, non-reciprocity of edge spin-plasmons induced by  $\mathbf{B}_z$  field may find potential applications in novel plasmonic or spintronic devices. In our future work, we want to study robustness of the gapless edge spin-plasmons against perturbations, such as a non-zero Rashba spin-mixing coupling or localized impurities on the edge [35]. Due to the spin-edge-locking of edge plasmons, We are interested in engineering spin-plasmons on different local edges via inhomogeneous substrate screening [55]. Moreover, we are also interested in further exploring plasmons, or other types of electronic collective excitations, in a three-dimensional topological system, such as Bernevig-Hughes-Zhang (BHZ) model [60].

## ACKNOWLEDGMENTS

We wish to acknowledge useful discussions with Chunyu Tan. Zhihao Jiang acknowledges the US Department of Energy, Office of Science, Materials Science and Engineering Division (under Contract No. DE-SC0022060) for supporting part of the manuscript preparation.

### Appendix A: Topological origin of gapless edge plasmons in Kane-Mele ribbon structure

We have observed high-energy bulk plasmons as well as gapless edge plasmons in the QSH phase of the Kane-Mele ribbon structure from the dispersions shown in Fig. 10(a). Here we demonstrate that these gapless edge plasmons have topological origin in the sense that they are directly originated from topological conducting edge states in the single-electron band structure. To this end, we apply the method of decomposing the full polarization function, denoted as  $\chi_0^{\text{full}}$ , into the edge part (involving transitions only within conducting edge bands) denoted as  $\chi_0^{\text{edge}}$  and the rest part involving other bulk bands.

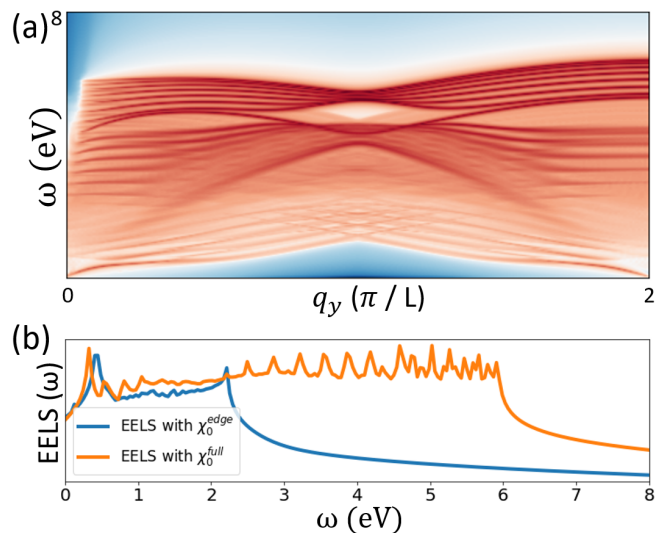


FIG. 10. (a) Plasmon dispersions of the Kane-Mele ribbon in the QSH phase. (b) Electron energy loss spectrum, i.e.  $EELS(q_y = \pi/8L, \omega)$ , of the Kane-Mele ribbon in the QSH phase evaluated with full susceptibility  $\chi_0^{\text{full}}$  and edge bands susceptibility  $\chi_0^{\text{edge}}$ , respectively.

Such a decomposition has been introduced in [35] in order to disentangle the bulk-states and edge-states contributions to plasmonic excitations in a topologically non-trivial system. In Fig. 10(b) we show the  $EELS(\omega, q_y)$  for the QSH phase at a small momentum transfer  $q_y = \pi/8L$ , using  $\chi_0^{\text{full}}$  and  $\chi_0^{\text{edge}}$  respectively. Comparing both spectra, we can see that  $\chi_0^{\text{edge}}$  qualitatively reproduces the low-energy part ( $\omega < 2.5$  eV) of the full spectrum with the full polarization  $\chi_0^{\text{full}}$  considered. This indicates that the low-energy plasmonic excitations are dominated by electronic edge states. As we have already confirmed in the main text, both conducting electronic states and gapless plasmon modes are strongly localized along the edge of the ribbon. Therefore, gapless edge plasmons indeed have topological origin.

### Appendix B: Plasmons in a large-bulk-gap QSH Kane-Mele ribbon with external magnetic field $\mathbf{B}_z$

We parameterize a QSH Kane-Mele ribbon with a large bulk band gap by increasing the diagonal spin-orbit coupling to  $t_{\text{SO}} = 0.15t$  (Eq. (6)). This makes bulk energy bands to be further away from conducting edge states at the Fermi level. In this scenario, a small external magnetic field  $\mathbf{B}_z$  will shift energy bands, but will not significantly affect the edge plasmon excitation and real-space localization. In Fig. 11(a) we show the EELS along  $q_y = \pi/8L$  (same as the one in the main text) for different strength of the magnetic field  $\mathbf{B}_z$ . As we can see, the edge plasmon excitation energy does not change very much, and its real-space charge modulation patterns for both spin components are still strongly localized at the

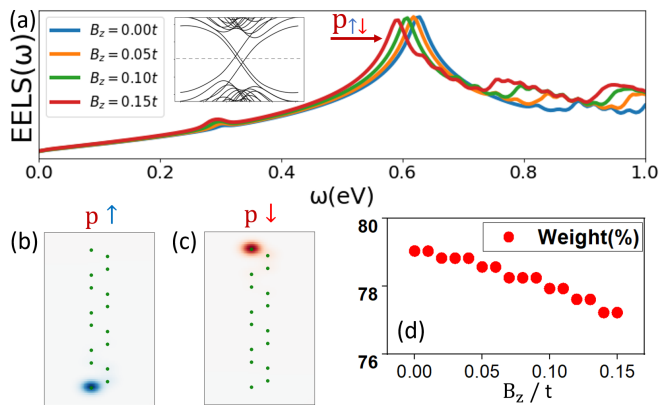


FIG. 11. (a) EELS of the QSH Kane-Mele model along the momentum transfer  $q_y = \pi/8L$  in the presence of external magnetic field  $\mathbf{B}_z$  of different strengths. Spin-orbit interaction in the numerical calculation here is  $t_{\text{SO}} = 0.15t$ . The inset shows the electronic band structure with  $B_z = 0.15t$ . (b) and (c) are real-space charge modulation patterns of two spin-plasmons excited at “P” with  $B_z = 0.15t$ . They are still strongly localized on edges. (d) shows a slightly decreasing weight of charges on the edge for the plasmon mode “P” with increased strength of the field.

edges of the ribbon. A quantitative description of the edge charge weight with increasing magnetic field up to  $B_z = 0.15t$  is shown in Fig. 11(d). We can see the maximum change is only about 2%. In this situation, edge plasmons are quite insensitive to the external magnetic field  $\mathbf{B}_z$ .

### Appendix C: Plasmonic excitations in the graphene-like honeycomb lattice

Instead of only discussing topological insulators, plasmonics has been investigated in different materials like graphene[61, 62] and  $\alpha\text{-T}_3$  model [63, 64]. In this section, we will analyze plasmons in a graphene-like model with a simple zigzag nano-ribbon (ZNR) structure as a compared benchmark, considering the tight-binding Hamiltonian,

$$\hat{H} = t \sum_{\langle i,j \rangle} c_i^\dagger c_j, \quad (\text{C1})$$

where  $\langle i, j \rangle$  represents nearest neighbor sites on the honeycomb lattice, and  $t$  is the corresponding hopping parameter. In Fig.12 we show results for a nanoribbon with 16 atoms in the unit cell. We first inspect the single particle energy bands, shown in Fig.12(a), and wave functions at particular momenta, shown in Figs.12(b) and (c). The finite size of the nanoribbon produces confinement of the electronic states in the regions near the Dirac points. The two bands in the gap overlap to form a state around  $K/L = \pi$ . By plotting the combined wave functions, we find that these zero-energy states in Fig.12(c) localize at the edges of the strip-like unit cell, whereas the other,

higher energy, wave functions at the same momentum are confined to the bulk. The two bands of the localized edge states that occur between  $\mathbf{K}$  and  $\mathbf{K}'$  in Fig.12(a) are affected twofold by the finite width, i.e., they merge and are slightly offset from zero[65].

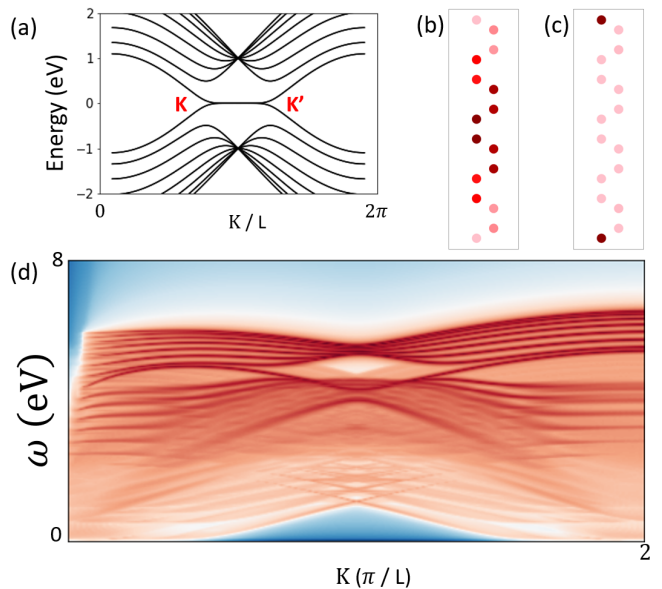


FIG. 12. (a): Single particle energy spectrum of the tight-binding nano-ribbon with zigzag edges. (b)-(c): Probability density of two wave functions ( $|\psi|^2$ ) at momentum  $K = \pi/L$ . (d): Electron energy loss spectrum (EELS) of the ribbon structure in the first Brillouin zone with periodic boundary in the X direction (parallel to the edges) and open boundaries in the Y direction (perpendicular to edges).

We now examine plasmonic excitations in this basic model and calculate the EELS along the Y-direction in momentum space while accounting for the spin degeneracy. Fig.12(d) shows the EELS in the first Brillouin zone, where we observe clusters of plasmonic branches in different energy regions. At high energies ( $\omega > 5$  eV), there are 8 plasmonic bands corresponding to the 8 A-sites in the unit cell. Similarly, there are also 8 plasmonic bands at intermediate energies ( $\omega \in \{2$  eV, 5 eV $\}$ ), including an arrow-shaped band at the exact center of the first Brillouin zone. In the low energy region ( $\omega < 2$  eV), we observe a continuum of excitations as well as several quasi-bands. By analyzing the single particle energy structure and the EELS of the ribbon, we conclude that the bulk energy bands and the geometry of the model are the original source of the high and intermediate energy plasmonic excitations. In contrast, the low energy continuum is due to the edge modes.

### Appendix D: Effects of small Rashba hopping on the edge plasmons

For the calculations in the main text, we set the Rashba term  $t_R = 0$  in the Kane-Mele model Hamiltonian [6],

which allows us to simply tune the phase of the model by the ratio of  $t_{SO}$  and  $t_v$ . In fact, according to the phase diagram of the QSH insulator (Fig.1 in [4]), a sufficiently small Rashba term does not change the phase of the system, and therefore has limited impact on gapless edge plasmons as well. Here we demonstrate this point by evaluating plasmonic dispersions in Kane-Mele model with a small Rashba term  $t_R = 0.05t$  while the system remains in the QSH phase ( $t_{SO} = 0.05t$ ,  $t_v = 0.1t$ ).

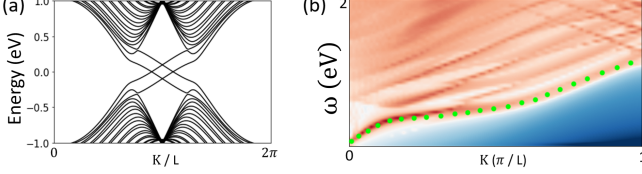


FIG. 13. (a) Electronic band structure of the Kane-Mele model on a ribbon with zigzag terminations for  $t_{SO} = 0.05t$ ,  $t_v = 0.1t$ , and a non-zero Rashba hopping  $t_R = 0.05t$ . (b) Electron energy loss spectra (EELS) of the same model. Green dots depict the plasmon dispersion without the Rashba hopping term for comparison.

In Fig. 13, we can see that both the single-electron band structure and the plasmon dispersions are barely affected by this small Rashba term, comparing to the situation with zero Rashba coupling in the main text (Figs. 2 and 3). For better comparison, we show green dots in Fig 13(b) representing the dispersion of edge plasmons without Rashba term. The dispersion nearly overlaps with the situation of non-zero Rashba hopping  $t_R = 0.05t$ . We therefore conclude that a sufficiently small Rashba hopping does not significantly change the single electron spectrum and plasmon dispersions.

### Appendix E: Symmetries of Kane-Mele model with and without external magnetic field

In this section we briefly show some relevant symmetry operations applied to the models we have discussed in the main text.

(1) Time reversal (TR) symmetry of the Kane-Mele model: we consider the Hamiltonian (6) written in the spin basis as

$$H = \begin{pmatrix} H_{\uparrow\uparrow} & H_{\uparrow\downarrow} \\ H_{\downarrow\uparrow} & H_{\downarrow\downarrow} \end{pmatrix} \quad (\text{E1})$$

where

$$H_{\uparrow\uparrow} = t \sum_{\langle i,j \rangle} c_i^\dagger c_j + it_{SO} \sum_{\langle\langle i,j \rangle\rangle} \nu_{ij} c_i^\dagger c_j + t_v \sum_i \xi_i c_i^\dagger c_i, \quad (\text{E2})$$

$$H_{\downarrow\downarrow} = t \sum_{\langle i,j \rangle} c_i^\dagger c_j - it_{SO} \sum_{\langle\langle i,j \rangle\rangle} \nu_{ij} c_i^\dagger c_j + t_v \sum_i \xi_i c_i^\dagger c_i, \quad (\text{E3})$$

$$H_{\uparrow\downarrow} = -t_R \sum_{\langle i,j \rangle} \tilde{d}_{ij} c_i^\dagger c_j, \quad (\text{E4})$$

$$H_{\downarrow\uparrow} = t_R \sum_{\langle i,j \rangle} \tilde{d}_{ij}^* c_i^\dagger c_j. \quad (\text{E5})$$

Here  $\tilde{d}_{ij} = d_{ij}^x - id_{ij}^y$  and “\*” indicates complex conjugation. We notice that  $H_{\uparrow\uparrow} = H_{\downarrow\downarrow}^*$  and  $H_{\uparrow\downarrow} = -H_{\downarrow\uparrow}^*$ . Now we apply TR operator  $\mathcal{T} = i\sigma_y \mathcal{K}$  to the Hamiltonian (E1) and we get

$$\mathcal{T} \begin{pmatrix} H_{\uparrow\uparrow} & H_{\uparrow\downarrow} \\ H_{\downarrow\uparrow} & H_{\downarrow\downarrow} \end{pmatrix} \mathcal{T}^{-1} = \begin{pmatrix} H_{\downarrow\downarrow}^* & -H_{\downarrow\uparrow}^* \\ -H_{\uparrow\downarrow}^* & H_{\uparrow\uparrow}^* \end{pmatrix} = H. \quad (\text{E6})$$

The Kane-Mele model Hamiltonian (6) is TR invariant. (2) Broken TR symmetry by the  $B_z$  field: we consider the additional term in the Hamiltonian due to the external field in  $z$ -direction which is  $\sum_i c_i^\dagger B_z s_z c_i$ . This term breaks the TR symmetry because

$$\mathcal{T} \sigma_z \mathcal{T}^{-1} = i\sigma_y \mathcal{K} \sigma_z (-i)\sigma_y \mathcal{K} = \sigma_y \sigma_z \sigma_y = -\sigma_z. \quad (\text{E7})$$

(3) Broken TR symmetry by the  $B_x$  field: we consider the additional term in the Hamiltonian due to the external field in  $x$ -direction which is  $\sum_i c_i^\dagger B_x s_x c_i$ . This term breaks the TR symmetry because

$$\mathcal{T} \sigma_x \mathcal{T}^{-1} = i\sigma_y \mathcal{K} \sigma_x (-i)\sigma_y \mathcal{K} = \sigma_y \sigma_x \sigma_y = -\sigma_x. \quad (\text{E8})$$

(4) Broken  $\mathcal{M}_y$  symmetry by the  $B_z$  field: in our ribbon structure with zigzag edges (Fig. 1), the mirror reflection  $\mathcal{M}_y$  does not change the type of sub-lattice but just flips the spin. The Zeeman energy term due to  $B_z$  is

$$H_z = \sum_i c_i^\dagger B_z s_z c_i = B_z \sum_i (c_{i\uparrow}^\dagger c_{i\uparrow} - c_{i\downarrow}^\dagger c_{i\downarrow}). \quad (\text{E9})$$

$H_z$  becomes  $-H_z$  after mirror reflection  $\mathcal{M}_y$ .

(5) Preserved  $\mathcal{M}_y$  symmetry by the  $B_x$  field: the Zeeman energy term due to  $B_x$  is

$$H_x = \sum_i c_i^\dagger B_x s_x c_i = B_x \sum_i (c_{i\uparrow}^\dagger c_{i\downarrow} + c_{i\downarrow}^\dagger c_{i\uparrow}). \quad (\text{E10})$$

$H_x$  is invariant after mirror reflection  $\mathcal{M}_y$ .

[1] K. v. Klitzing, G. Dorda, and M. Pepper, New method for high-accuracy determination of the fine-structure con-

stant based on quantized hall resistance, Phys. Rev. Lett.

- 45**, 494 (1980).
- [2] D. J. Thouless, M. Kohmoto, M. P. Nightingale, and M. den Nijs, Quantized hall conductance in a two-dimensional periodic potential, *Phys. Rev. Lett.* **49**, 405 (1982).
- [3] F. D. M. Haldane, Model for a quantum hall effect without landau levels: Condensed-matter realization of the "parity anomaly", *Phys. Rev. Lett.* **61**, 2015 (1988).
- [4] C. L. Kane and E. J. Mele,  $Z_2$  topological order and the quantum spin hall effect, *Phys. Rev. Lett.* **95**, 146802 (2005).
- [5] C. L. Kane and E. J. Mele, Quantum spin hall effect in graphene, *Phys. Rev. Lett.* **95**, 226801 (2005).
- [6] H. A. Kramers, Théorie générale de la rotation paramagnétique dans les cristaux, *Proc. Acad. Amst* **33** (1930).
- [7] D. Vanderbilt, *Berry phases in electronic structure theory: electric polarization, orbital magnetization and topological insulators* (Cambridge University Press, 2018).
- [8] Y. Zhang, Y. W. Tan, H. L. Stormer, and P. Kim, Experimental observation of the quantum Hall effect and Berry's phase in graphene, *Nature* **438**, 201 (2005).
- [9] B. A. Bernevig and S. C. Zhang, Quantum spin hall effect, *Physical Review Letters* **96**, 106802 (2006).
- [10] B. A. Bernevig, T. L. Hughes, and S. C. Zhang, Quantum spin hall effect and topological phase transition in HgTe quantum wells, *Science* **314**, 1757 (2006).
- [11] M. König, S. Wiedmann, C. Brüne, A. Roth, H. Buhmann, L. W. Molenkamp, X. L. Qi, and S. C. Zhang, Quantum spin hall insulator state in HgTe quantum wells, *Science* **318**, 766 (2007).
- [12] K. S. Novoselov, Z. Jiang, Y. Zhang, S. V. Morozov, H. L. Stormer, U. Zeitler, J. C. Maan, G. S. Boebinger, P. Kim, and A. K. Geim, Room-temperature quantum hall effect in graphene, *Science* **315**, 1379 (2007).
- [13] L. Fu, C. L. Kane, and E. J. Mele, Topological insulators in three dimensions, *Physical Review Letters* **98**, 106803 (2007).
- [14] L. Fu and C. L. Kane, Topological insulators with inversion symmetry, *Physical Review B* **76**, 045302 (2007).
- [15] D. Hsieh, D. Qian, L. Wray, Y. Xia, Y. S. Hor, R. J. Cava, and M. Z. Hasan, A topological Dirac insulator in a quantum spin Hall phase, *Nature* **452**, 970 (2008).
- [16] Y. L. Chen, J. G. Analytis, J. H. Chu, Z. K. Liu, S. K. Mo, X. L. Qi, H. J. Zhang, P. H. Lu, X. Dai, Z. Fang, S. C. Zhang, I. R. Fisher, Z. Hussain, and Z. X. Shen, Experimental realization of a three-dimensional topological insulator, Bi<sub>2</sub>Te<sub>3</sub>, *Science* **325**, 178 (2009).
- [17] K. Kuroda, M. Ye, A. Kimura, S. V. Eremeev, E. E. Krasovskii, E. V. Chulkov, Y. Ueda, K. Miyamoto, T. Okuda, K. Shimada, H. Namatame, and M. Taniguchi, Experimental realization of a three-dimensional topological insulator phase in ternary chalcogenide TlBiSe<sub>2</sub>, *Physical Review Letters* **105**, 146801 (2010).
- [18] Y. Gong, J. Guo, J. Li, K. Zhu, M. Liao, X. Liu, Q. Zhang, L. Gu, L. Tang, X. Feng, D. Zhang, W. Li, C. Song, L. Wang, P. Yu, X. Chen, Y. Wang, H. Yao, W. Duan, Y. Xu, S. C. Zhang, X. Ma, Q. K. Xue, and K. He, Experimental Realization of an Intrinsic Magnetic Topological Insulator, *Chinese Physics Letters* **36**, 076801 (2019).
- [19] R. Noguchi, T. Takahashi, K. Kuroda, M. Ochi, T. Shirasawa, M. Sakano, C. Bareille, M. Nakayama, M. D. Watson, K. Yaji, A. Harasawa, H. Iwasawa, P. Dudin, T. K. Kim, M. Hoesch, V. Kandyba, A. Giampietri, A. Barinov, S. Shin, R. Arita, T. Sasagawa, and T. Kondo, A weak topological insulator state in quasi-one-dimensional bismuth iodide, *Nature* **566**, 518 (2019).
- [20] A. Karch, Surface plasmons and topological insulators, *Phys. Rev. B* **83**, 245432 (2011).
- [21] Y. Okada and V. Madhavan, Topological insulators: plasmons at the surface, *Nature nanotechnology* **8**, 541 (2013).
- [22] R. Schütty, C. Ertler, A. Trügler, and U. Hohenester, Surface plasmons in doped topological insulators, *Physical Review B* **88**, 195311 (2013).
- [23] D. K. Efimkin, Y. E. Lozovik, and A. A. Sokolik, Collective excitations on a surface of topological insulator, *Nanoscale Research Letters* 10.1186/1556-276X-7-163 (2012).
- [24] J. Yuan, W. Ma, L. Zhang, Y. Lu, M. Zhao, H. Guo, J. Zhao, W. Yu, Y. Zhang, K. Zhang, H. Y. Hoh, X. Li, K. P. Loh, S. Li, C. W. Qiu, and Q. Bao, Infrared Nanoimaging Reveals the Surface Metallic Plasmons in Topological Insulator, *ACS Photonics* **4**, 3055 (2017).
- [25] A. M. Dubrovkin, G. Adamo, J. Yin, L. Wang, C. Soci, Q. J. Wang, and N. I. Zheludev, Visible Range Plasmonic Modes on Topological Insulator Nanostructures, *Advanced Optical Materials* **5**, 1600768 (2017).
- [26] D. Jin, T. Christensen, M. Soljačić, N. X. Fang, L. Lu, and X. Zhang, Infrared Topological Plasmons in Graphene, *Physical Review Letters* **118**, 245301 (2017).
- [27] P. Di Pietro, M. Ortolani, O. Limaj, A. Di Gaspere, V. Giliberti, F. Giorgianni, M. Brahlek, N. Bansal, N. Koirala, S. Oh, P. Calvani, and S. Lupi, Observation of Dirac plasmons in a topological insulator, *Nature Nanotechnology* **8**, 556 (2013).
- [28] P. K. Venuthurumilli, X. Wen, V. Iyer, Y. P. Chen, and X. Xu, Near-Field Imaging of Surface Plasmons from the Bulk and Surface State of Topological Insulator Bi<sub>2</sub>Te<sub>2</sub>Se, *ACS Photonics* **6**, 2492 (2019).
- [29] Y. P. Lai, I. T. Lin, K. H. Wu, and J. M. Liu, Plasmonics in topological insulators (2014).
- [30] T. P. Ginley and S. Law, Coupled Dirac Plasmons in Topological Insulators, *Advanced Optical Materials* **6**, 1800113 (2018).
- [31] A. Rückriegel, A. Brataas, and R. A. Duine, Bulk and edge spin transport in topological magnon insulators, *Physical Review B* **97**, 081106 (2018).
- [32] M. Malki and G. S. Uhrig, Topological magnon bands for magnonics, *Physical Review B* **99**, 174412 (2019).
- [33] A. Mook, J. Henk, and I. Mertig, Edge states in topological magnon insulators, *Physical Review B* **90**, 024412 (2014).
- [34] Z. Jiang, M. Rösner, R. E. Groenewald, and S. Haas, Localized plasmons in topological insulators, *Phys. Rev. B* **101**, 045106 (2020).
- [35] Y. Guan, Z. Jiang, and S. Haas, Control of plasmons in topological insulators via local perturbations, *Phys. Rev. B* **104**, 125425 (2021).
- [36] H. Schlömer, Z. Jiang, and S. Haas, Plasmons in two-dimensional topological insulators, *Phys. Rev. B* **103**, 115116 (2021).
- [37] D. K. Efimkin and M. Kargarian, Topological spin-plasma waves, *Phys. Rev. B* **104**, 075413 (2021).
- [38] I. Appelbaum, H. D. Drew, and M. S. Fuhrer, Proposal for a topological plasmon spin rectifier, *Applied Physics Letters* **98**, 10.1063/1.3541545 (2011).

- [39] A. Agarwal, M. Polini, G. Vignale, and M. E. Flatté, Long-lived spin plasmons in a spin-polarized two-dimensional electron gas, *Phys. Rev. B* **90**, 155409 (2014).
- [40] A. Agarwal and G. Vignale, Plasmons in spin-polarized graphene: A way to measure spin polarization, *Phys. Rev. B* **91**, 245407 (2015).
- [41] Y. Ren, Z. Qiao, and Q. Niu, Engineering corner states from two-dimensional topological insulators, *Phys. Rev. Lett.* **124**, 166804 (2020).
- [42] D. Pines and D. Bohm, A collective description of electron interactions: Ii. collective vs individual particle aspects of the interactions, *Phys. Rev.* **85**, 338 (1952).
- [43] D. Bohm and D. Pines, A collective description of electron interactions: Iii. coulomb interactions in a degenerate electron gas, *Phys. Rev.* **92**, 609 (1953).
- [44] W. Wang, T. Christensen, A.-P. Jauho, K. S. Thygesen, M. Wubs, and N. A. Mortensen, Plasmonic eigenmodes in individual and bow-tie graphene nanotriangles, *Scientific Reports* **5**, 9535 (2015).
- [45] T. Westerhout, E. van Veen, M. I. Katsnelson, and S. Yuan, Plasmon confinement in fractal quantum systems, *Phys. Rev. B* **97**, 205434 (2018).
- [46] We want to clarify that this is a simplified assumption. The density-density Coulomb interaction can depend on electron spin especially when the real-space distance is small, however, this is out of the scope of the current paper and will be considered in future works.
- [47] B. Santoyo, Plasmons in three, two and one dimension, *Revista Mexicana de Fisica* **39**, 640 (1993).
- [48] D. Huertas-Hernando, F. Guinea, and A. Brataas, Spin-orbit coupling in curved graphene, fullerenes, nanotubes, and nanotube caps, *Phys. Rev. B* **74**, 155426 (2006).
- [49] H. Min, J. E. Hill, N. A. Sinitsyn, B. R. Sahu, L. Kleinman, and A. H. MacDonald, Intrinsic and rashba spin-orbit interactions in graphene sheets, *Phys. Rev. B* **74**, 165310 (2006).
- [50] Y. Yao, F. Ye, X.-L. Qi, S.-C. Zhang, and Z. Fang, Spin-orbit gap of graphene: First-principles calculations, *Phys. Rev. B* **75**, 041401 (2007).
- [51] J. C. Boettger and S. B. Trickey, First-principles calculation of the spin-orbit splitting in graphene, *Phys. Rev. B* **75**, 121402 (2007).
- [52] A. Varykhalov, J. Sánchez-Barriga, A. M. Shikin, C. Biswas, E. Vescovo, A. Rybkin, D. Marchenko, and O. Rader, Electronic and magnetic properties of quasifreestanding graphene on ni, *Phys. Rev. Lett.* **101**, 157601 (2008).
- [53] N. Tombros, S. Tanabe, A. Veligura, C. Jozsa, M. Popinciuc, H. T. Jonkman, and B. J. van Wees, Anisotropic spin relaxation in graphene, *Phys. Rev. Lett.* **101**, 046601 (2008).
- [54] A. Bansil, H. Lin, and T. Das, Colloquium: Topological band theory, *Reviews of Modern Physics* **88**, 10.1103/RevModPhys.88.021004 (2016).
- [55] Z. Jiang, S. Haas, and M. Rösner, Plasmonic waveguides from coulomb-engineered two-dimensional metals, *2D Materials* **8**, 10.1088/2053-1583/abfedd (2021).
- [56] K. Maiti, J. Fink, S. de Jong, M. Gorgoi, C. Lin, M. Raichle, V. Hinkov, M. Lambacher, A. Erb, and M. S. Golden, Doping dependence of the chemical potential and surface electronic structure in  $\text{yba}_2\text{cu}_3\text{o}_{6+x}$  and  $\text{la}_{2-x}\text{sr}_x\text{cuo}_4$  using hard x-ray photoemission spectroscopy, *Phys. Rev. B* **80**, 165132 (2009).
- [57] N. L. Wang, G. Li, D. Wu, X. H. Chen, C. H. Wang, and H. Ding, Doping evolution of the chemical potential, spin-correlation gap, and charge dynamics of  $\text{nd}_{2-x}\text{ce}_x\text{CuO}_4$ , *Phys. Rev. B* **73**, 184502 (2006).
- [58] H.-M. Christen, J. Mannhart, E. J. Williams, and C. Gerber, Dielectric properties of sputtered  $\text{srtio}_3$  films, *Phys. Rev. B* **49**, 12095 (1994).
- [59] Q. Wang, H. Yao, Y. Feng, X. Deng, B. Yang, D. Xiong, M. He, and W. Zhang, Surface plasmon resonances boost the transverse magneto-optical kerr effect in a cofeb slab covered by a subwavelength gold grating for highly sensitive detectors, *Optics Express* **29**, 10.1364/oe.414749 (2021).
- [60] B. A. Bernevig, T. L. Hughes, and S.-C. Zhang, Quantum spin hall effect and topological phase transition in hgte quantum wells, *Science* **314**, 1757 (2006).
- [61] O. L. Berman, G. Gumbs, and Y. E. Lozovik, Magneto-plasmons in layered graphene structures, *Phys. Rev. B* **78**, 085401 (2008).
- [62] O. L. Berman, R. Y. Kezerashvili, and Y. E. Lozovik, Graphene-based photonics and plasmonics, in *Nanoscale Materials and Devices for Electronics, Photonics and Solar Energy*, edited by A. Korokin, S. Goodnick, and R. Nemanich (Springer International Publishing, Cham, 2015) pp. 93–126.
- [63] A. Iurov, L. Zhemchuzhna, G. Gumbs, D. Huang, D. Dahal, and Y. Abranyos, Finite-temperature plasmons, damping, and collective behavior in the  $\alpha - \mathbf{t}_3$  model, *Phys. Rev. B* **105**, 245414 (2022).
- [64] A. Iurov, L. Zhemchuzhna, G. Gumbs, D. Huang, P. Fekete, F. Anwar, D. Dahal, and N. Weekes, Tailoring plasmon excitations in  $\alpha - \mathbf{t}_3$  armchair nanoribbons, *Scientific Reports* **11**, 10.1038/s41598-021-99596-z (2021).
- [65] L. Brey and H. A. Fertig, Electronic states of graphene nanoribbons studied with the dirac equation, *Phys. Rev. B* **73**, 235411 (2006).